AGU PUBLICATIONS

JGR

Journal of Geophysical Research: Oceans

RESEARCH ARTICLE

10.1002/2016JC012640

Impact of data assimilation on Eulerian versus Lagrangian estimates of upper ocean transport

Ann Kristin Sperrevik[1], Johannes Röhrs[1], and Kai Håkon Christensen[1]

[1]Norwegian Meteorological Institute, Oslo, Norway

Key Points:
- Improving stratification through 4D-Var DA changes the effective model resolution
- Eulerian kinetic energy levels remain the same before and after DA
- Lagrangian kinetic energy levels are changed after DA

Correspondence to:
A. K. Sperrevik,
annks@met.no

Citation:
Sperrevik, A. K., J. Röhrs, and K. H. Christensen (2017), Impact of data assimilation on Eulerian versus Lagrangian estimates of upper ocean transport, *J. Geophys. Res. Oceans*, *122*, 5445–5457, doi:10.1002/2016JC012640.

Received 19 DEC 2016
Accepted 7 JUN 2017
Accepted article online 9 JUN 2017
Published online 7 JUL 2017

Abstract Using four-dimensional variational analysis, we produce an estimate of the state of a coastal region in Northern Norway during the late winter and spring in 1984. We use satellite sea surface temperature and in situ observations from a series of intensive field campaigns, and obtain a more realistic distribution of water masses both in the horizontal and the vertical than a pure downscaling approach can achieve. Although the distribution of Eulerian surface current speeds are similar, we find that they are more variable and less dependent on model bathymetry in our reanalysis compared to a hindcast produced using the same modeling system. Lagrangian drift currents on the other hand are significantly changed, with overall higher kinetic energy levels in the reanalysis than in the hindcast, particularly in the superinertial frequency band.

1. Introduction

Modeling the transport of plankton, pollution, and drifting objects presents an ongoing challenge in operational oceanography. To obtain realistic Lagrangian trajectories, circulation models need to resolve the horizontal structure of the time-varying currents as well as correctly describe the vertical dynamical balances that determine the vertical position or distribution of the quantity of interest. Shelf and coastal seas are of particular interest as human activity is concentrated near the coast, and shelf seas are most relevant for primary production, fisheries, and oil exploitation.

Ocean circulation models set up for a specific coastal or shelf sea are commonly used to provide the Eulerian current fields used for Lagrangian transport studies. Such regional ocean circulation models crucially depend on initial and boundary conditions from coarser models, which may lack important details relevant for the specific region. Increasing the model resolution usually implies better physics as more processes and scales are resolved, but errors propagating in from parent grids reduces model skill. Traditionally, ocean model errors have mainly been associated with initialization, and errors due to the boundary conditions have been most pronounced in limited area numerical weather prediction (NWP) models [e.g., *Warner et al.*, 1997]. Such limitations in predictability due to the boundary conditions are becoming increasingly relevant in the high-resolution ocean models used for coastal applications.

One way to improve a regional ocean model is through data assimilation (DA), combining observations and model fields in an optimal way to provide the best possible estimate of the true state. Ocean DA is rapidly developing as advanced methods are inherited from NWP and adapted to ocean circulation models. For instance, the four-dimensional variational analysis scheme used in this study [*Moore et al.*, 2011a,2011b,2011c] uses linear model physics to propagate information in time, which allows the model state to be adjusted in a dynamically consistent way, even though the observations are not taken at the analysis time. In addition, the analysis scheme allows for corrections of errors in the lateral boundary conditions and the surface forcing.

Particle transport crucially depends on transient current features such as tides and eddies. To realistically resolve the small-scale transient currents, it is not only required that the ocean model has sufficient spatial resolution, but also that the model has a correct water mass distribution in order to resolve frontal instabilities and the baroclinic response to large-scale forcing.

The focus region in this work is the Lofoten and Vesterålen shelf sea in northern Norway (see Figure 1), where we find the primary spawning ground for Northeast Arctic Cod (*Gadus morhua*) in addition to rich oil

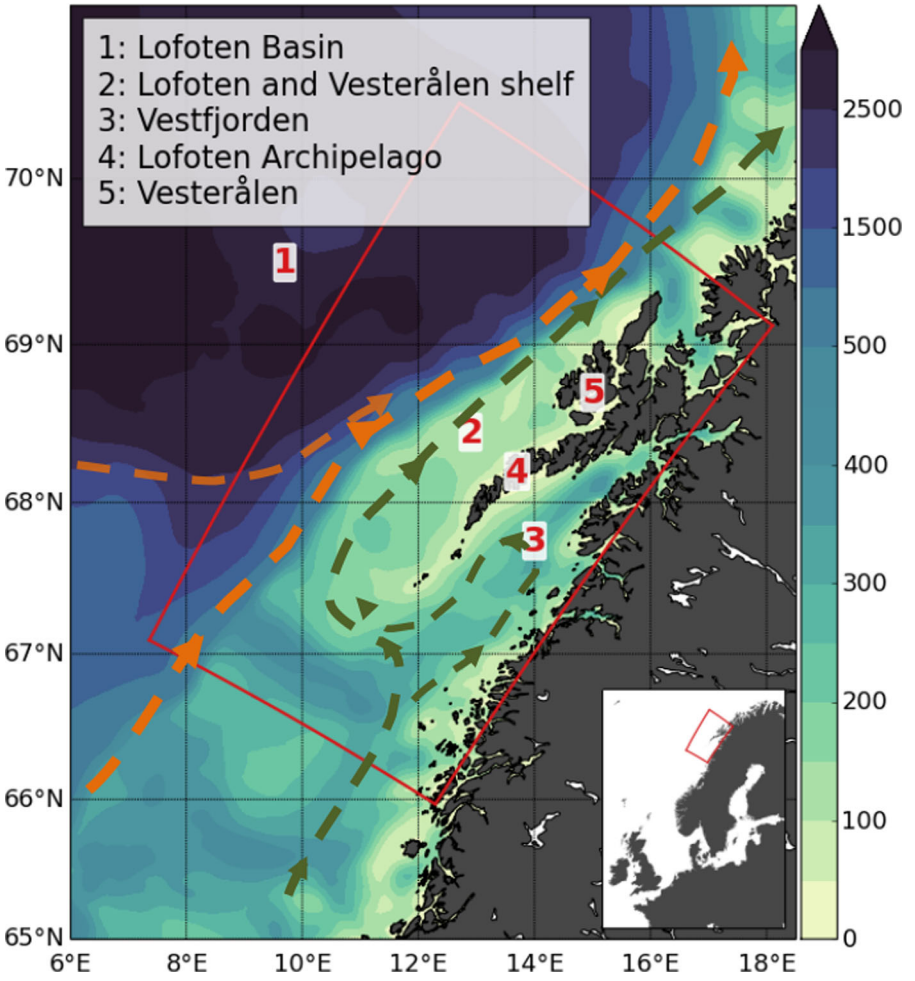

Figure 1. Study area in Northern Norway. Ocean depth is illustrated by shading, while the red box indicates the model domain. The overall pathways of the Norwegian Atlantic Current and the Norwegian Coastal Current are indicated in orange and green, respectively.

and gas reservoirs. Cod eggs spawned in Vestfjorden are transported with the Norwegian Coastal Current and the Norwegian Atlantic Current to the nursery grounds in the Barents Sea. The Lofoten and Vesterålen area has so far been protected from oil and gas exploitation as a preventive measure, but the continuation of this state of affairs remains uncertain. Previous studies of transport processes in this region have focused on connectivity (primarily cod egg and larvae transport), oil spill drift modeling, and marine ecosystem models [e.g., *Svendsen et al*., 2007; *Vikebø et al*., 2013; *Eide et al*., 2007; *De Hoop et al*., 2016].

The large-scale pathways of zooplankton and ichtyoplankton from the Lofoten and Vesterålen shelf sea northward to the Barents Sea are generally known [*Ådlandsvik and Sundby*, 1994; *Vikebø et al*., 2007]. Recently, the focus has turned to smaller scales and the upper ocean dynamics that impact on particle transport near the coast. Particularly interesting for this study is the work of *Myksvoll et al*. [2014], who demonstrate the impact of vertical stratification. The eggs of the Coastal cod are denser than the Northeast Arctic cod eggs, and hence have a different distribution with depth, resulting in a retention of Coastal cod eggs near the coast. Field studies using different types of drifters also demonstrate a remarkable variation in the drift currents with depth, implying that the direct impact of the atmospheric forcing on the transport diminishes very rapidly away from the surface [*Röhrs and Christensen*, 2015]. Previous studies thus point to two different aspects of the role of stratification for the transport: (i) the role of stratification for the vertical distribution of buoyant particles, and (ii) the role of stratification for the intrinsic ocean response to atmospheric forcing. It is the second point that we will focus on here, and we will compare our results to a downscaled version of the SVIM hindcast archive, which has been used in several previous transport studies in this region [*Langangen et al*., 2016; *Stige et al*., 2015; *Kvile et al*., 2016].

We present a reanalysis of the Lofoten and Vesterålen shelf sea circulation made with a four-dimensional variational DA scheme. The hydrographic observations are taken from a series of intensive field campaigns in 1984 [*Sundby and Bratland*, 1987] and from reprocessed satellite sea surface temperature (SST) measurements. We emphasize on the impact of improved hydrography on the overall circulation and the Lagrangian transport statistics. The outline of the paper is as follows: In section 2 we briefly describe the oceanography of the Lofoten and Vesterålen shelf sea; in section 3 we describe the numerical model and the observations; in section 4 we summarize our results. Finally, section 5 contains a brief discussion and some concluding remarks.

2. The Lofoten and Vesterålen Shelf Sea

The shelf in northern Norway is bounded to the east by a mountainous coastline with deep fjords and numerous islands and skerries, and there is a steep shelf break toward the deep Norwegian Sea basin to the west. This shelf break controls a branch of the relatively warm and saline Norwegian Atlantic Current (NAC). On the inner part of the shelf we find the fresh and cold Norwegian Coastal Current (NCC), which contains the river runoff from all along the Norwegian coast and freshwater originating in the Baltic Sea.

The Vesterålen shelf sea off the Lofoten and Vesterålen archipelago (Figure 1) is the narrowest part of the Norwegian shelf, being about 60 km wide. On this part of the shelf, the NAC and the NCC converge, giving rise to baroclinic instabilities and eddies shedding off to the Lofoten Basin [*Poulain et al*., 1996; *Volkov et al*., 2015; *Isachsen*, 2015]. On the inner part of the shelf, a branch of the NCC enters Vestfjorden, a wide bay separated from the surrounding shelf sea by a deep sill ($\sim$230 m) in the south and the Lofoten archipelago to the west. The outflow from Vestfjorden is primarily found on the western side, along the Lofoten archipelago. The general circulation pattern in Vestfjorden is cyclonic, occasionally interrupted by complex transient circulation patterns that develop in response to local winds.

The winds during winter and spring in Vestfjorden are often from northeast due to Katabatic flow of cold air from the mainland. These winds force near-surface water in Vestfjorden toward the outer part of the shelf. A second mode of wind-driven circulation is set up by southwesterly winds during the passage of low pressure systems. In such cases, the cyclonic circulation pattern in Vestfjorden is interrupted and water masses are retained in Vestfjorden and piled up toward the inner parts [*Ellertsen et al*., 1981; *Furnes and Sundby*, 1981]. The water flushes out when the wind drops, and is driven to the Lofoten and Vesterålen shelf by rotational effects. This interaction between Vestfjorden and the Lofoten and Vesterålen shelf is repeated throughout winter and spring, and is a source of great variability in the NCC.

The Vestfjorden bay is up to 500 m deep and below the surface layer there is remnant Atlantic water. The water in Vestfjorden is stably, albeit weakly, stratified: since the deeper Atlantic water is warmer than the coastal water, the temperature is often found to increase with depth. Depending on the wind situation, there is upwelling of Atlantic water along the rim of the bay, with southwesterly winds resulting in upwelling of Atlantic water toward the Lofoten archipelago. The stratification on the shelf and on the shelf slope depends on both the amount of fresh water advected by the coastal current, the wind and wave-induced mixing, and the amount of coastal upwelling and downwelling. The stratification exhibits a strong seasonal cycle both inside Vestfjorden and in the surrounding shelf sea. During late spring and summer, the stratification is enhanced due to increased runoff associated with snow melting, as well as solar heating of the surface layer, resulting in a wide and shallow NCC. In contrast, low runoff levels combined with surface cooling causes a deepening of the mixed layer during winter. In the cold season, the NCC thus becomes narrow and deep.

The most dominant tidal constituents are the semidiurnal lunar M2 component followed by the semidiurnal S2, while the largest diurnal component is the lunisolar K1 [*Moe et al*., 2002]. Very strong tidal flows in narrow sounds and shallow regions contribute to the coast-shelf exchange. The period of M2 (12.42 h) is close to the inertial period ($\sim$12.9) in this region, and both the tides and inertial oscillations add to the variability of currents around the Lofoten archipelago.

3. Models and Observations

In this study, we model an area centered around the archipelago of Lofoten and Vesterålen in Northern Norway (Figure 1), using a horizontal resolution of 2.4 km and 35 vertical levels. This setup have been used in previous

studies, assessing the impact of assimilating High Frequency radar observations on forecast skill [*Sperrevik et al*., 2015], and, at a higher resolution of 800 m, the impact of wave-current interactions and wave-induced mixing on the Lagrangian transport of cod eggs and larvae [*Röhrs et al*., 2014]. We will present results from two different model realizations: (i) a downscaling of the SVIM archive, denoted as SVIM-DS, [*Lien et al*., 2013, 2014] and (ii) a reanalysis denoted as ANA, generated by assimilation in situ hydrography and satellite SST.

3.1. Modeling System

The numerical ocean model used in this study is the Regional Ocean Modeling System (ROMS), which is a free-surface, hydrostatic, primitive equation model with terrain-following vertical coordinates [*Haidvogel et al*., 2008; *Shchepetkin and McWilliams*, 2005]. ROMS comes with a set of tools for strong and weak constraint four-dimensional variational (4D-Var) data assimilation, as well as a framework for assessing observation impacts and model sensitivities using adjoint techniques [*Moore et al*., 2004, 2011a, 2011b, 2011c]. In this study, we utilize the strong constraint, incremental 4D-Var driver (IS4DVAR) to perform state estimation.

In 4D-Var the aim is to adjust the model state over the course of a time interval—the assimilation window—in a way that minimizes a cost function defined as

$$J(\mathbf{x}) = \frac{1}{2}(\mathbf{x}-\mathbf{x}_b)^T\mathbf{B}^{-1}(\mathbf{x}-\mathbf{x}_b) + \frac{1}{2}(\mathbf{y}-H(\mathbf{x}))^T\mathbf{R}^{-1}(\mathbf{y}-H(\mathbf{x})). \quad (1)$$

Here, the model state variables and lateral boundary conditions are concatenated into the vector **x**, referred to as the control vector. $\mathbf{x}_b$ is a vector of the control variables of the background state, **y** is a vector containing the observations, **B** is the background error covariance matrix, **R** is the observation error covariance matrix, and H is an observation operator. In the case of 4D-Var, H includes the full nonlinear ocean model to facilitate temporal mapping of the observations. A solution $\mathbf{x}_a$, termed the analysis, is found by applying an iterative approach [*Courtier et al*., 1994], in which a tangent linear model version of ROMS and its adjoint is used to find increments to **x** that yields smaller values of the cost function.

3.2. The SVIM Downscaling

SVIM is a hindcast archive that covers the Nordic Seas and parts of the Arctic Ocean with a horizontal resolution of 4 km and with 32 vertical layers. The archive covers the time period from 1958 until present, being updated four times per year. To produce more detailed field of the ocean state in our region of interest, we performed a dynamical downscaling of the original SVIM fields by running ROMS at a higher resolution using the same atmospheric forcing as the original hindcast archive with 6 hourly fields of winds, temperature, humidity, mean sea level pressure, total cloud cover, and net precipitation from the Norwegian Reanalysis 10 km (NORA10) archive [*Reistad et al*., 2011]. Daily means of salinity, potential temperature, sea surface elevation, and barotropic and baroclinic velocities from the SVIM archive are used both for initial and boundary conditions. The boundary conditions are applied using a combination of radiation and nudging conditions as proposed by *Marchesiello et al*. [2001], while surface elevation and barotropic currents are imposed following the recommendations of *Flather* [1976] and *Chapman* [1985]. In addition, tidal forcing from the TPXO global inverse barotropic model of ocean tides [*Egbert and Erofeeva*, 2002] is applied. The model is also forced with daily estimates of river discharges from the Norwegian Water Resources and Energy Directorate [*Beldring et al*., 2001].

3.3. 4D-Var Reanalysis

The model configuration for the reanalysis is the same as for SVIM-DS, but due to limitations in the adjoint and tangent linear models used by IS4DVAR, clamped boundary conditions with a sponge layer are used for the baroclinic variables. The configuration of the IS4DVAR driver is similar to that of *Sperrevik et al*. [2015] with two exceptions: the assimilation window length is increased from 24 to 72 h, and the control vector now includes the lateral boundary conditions. The horizontal decorrelation scales for the initial conditions and boundary conditions were 10 and 100 km, respectively, while for the vertical decorrelation scales 30 m was used for both initial and lateral boundary conditions.

Variational DA techniques assume that the background error covariance matrix (**B**), which describes the error characteristics of the background state, is known. In IS4DVAR, the **B** matrix is estimated from a combination of a multivariate balance operator (not used here), a univariate covariance operator, and background error standard deviations provided in input files [*Moore et al*., 2011a]. Here we have used a 3 years hindcast simulation to estimate monthly values of background error standard deviations. To account for seasonal

changes in the stratification and the circulation patterns, the background error standard deviations provided to IS4DVAR for any given assimilation window is estimated by a weighted mean of the two monthly values of the months closest in time to the assimilation window.

A reanalysis covering the time period of 1 January to 30 June 1984 is constructed in the following manner: The initial conditions for 1 January are retrieved from SVIM-DS, and a best estimate of the ocean state over the 72 h assimilation window is found by running IS4DVAR. The updated ocean state at the end of this assimilation window is then used as initial conditions for the next assimilation window. This procedure is repeated until the simulation reaches 30 June, by which IS4DVAR has been run for a total of 61 ensuing assimilation windows.

This sequential data assimilation procedure generates a reanalysis that is dynamically consistent within each assimilation window. The transition between adjacent assimilation windows will, however, not be continuous since the solution within a window is optimized for the observations available during that given period. A continuous solution for the entire period is obtained by running the model using the same configuration as for SVIM-DS, but this simulation was forced by hourly values of the lateral boundary conditions as well as surface forcing obtained from the IS4DVAR solutions. In addition, we nudge temperature and salinity towards the corresponding fields from the IS4DVAR solutions with a time scale of 12 h to retain the improvements achieved during the IS4DVAR simulations. The continuous solution obtained by this method is in the following denoted ANA, and the results from the assimilative model all refer to this model realization.

3.4. Observations

Two different SST data sets are used in the reanalysis. The first is the global SST https://preview.overleaf.com/public/wvfhcmrqmcsb/images/7e84400d62bf522c90d3712141765b2e8e492057.jpeg analysis provided by the National Oceanic and Atmospheric Administration [*Reynolds et al*., 2007], which is produced by blending AVHRR data with in situ measurements, generating daily averages at a 0.25° spherical grid. The second is a regional SST analysis provided by the Danish Meteorological Institute (also daily averages, see *Høyer and She* [2007]). This product has a spatial resolution of 0.03° which is comparable to the resolution of our model, but it only covers the model domain up to 68°N. The coverage and resolution of the two products is illustrated in Figures 2a and 2b.

In situ observations of temperature and salinity were retrieved from the EN4 data set available from the UK Met Office [*Good et al*., 2013]. For the region of interest, the data set mainly consists of ship-borne CTD observations, collected during extensive cruises by the Institute of Marine Research during the spring months [*Sundby and Bratland*, 1987]. As can be seen in Figures 2c and 2d, the observations are mainly from inside Vestfjorden and the Lofoten and Vesterålen shelf. In total there are 1272 profiles, taken as unique observation points with five or more measurements in the vertical, available during the period of the reanalysis. Figure 2e shows the temporal distribution of in situ observations.

4. Impact of State Estimation

4.1. Water Mass Distribution

The two model simulations, SVIM-DS and ANA, are compared by evaluating error statistics with respect to the in situ observations, which to a large extent are taken inside Vestfjorden and on the Lofoten and Vesterålen shelf, and hence mainly in coastal waters. Close to 90% of the observations are taken in the upper 100 meters of the water column, thus the ocean below the mixed layer is poorly sampled. Independent observations are not available since all the in situ profiles have been used in the reanalysis to provide maximum constraint on the model [e.g., *Janeković et al*., 2013].

Figure 3a shows a T-S diagram of all in situ observations of temperature and salinity along with the corresponding values from the two model simulations. To aid in the interpretation of the diagram, the Figures 3b–3e show root-mean-square errors (RMSE) and bias for temperature and salinity as a function of depth. The diagram shows that SVIM-DS is too saline and cold, and has much less variation than the observations. SVIM-DS thus resembles the original SVIM hindcast, in which the NCC have a strong positive salinity bias [*Lien et al*., 2013]. In contrast, the cold and saline deep water is well reproduced.

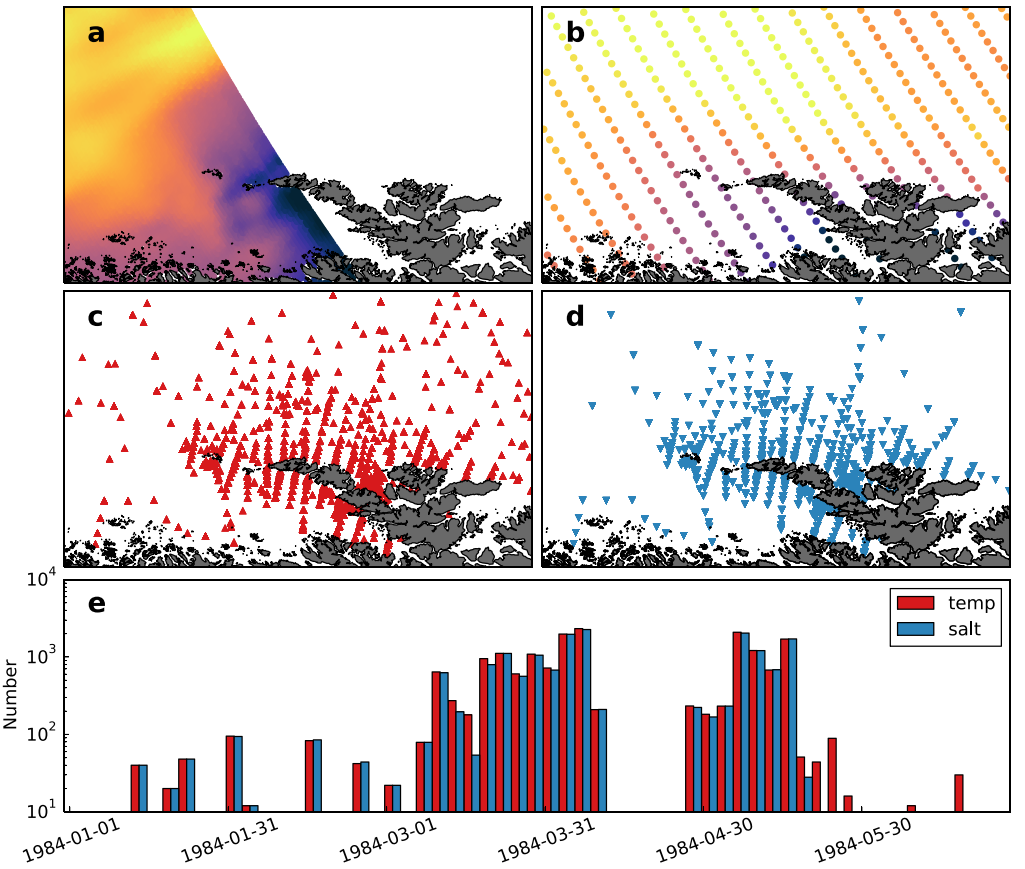

Figure 2. SST for 15 April 1984 from (a) DMI and (b) NOAA. All in situ (c) temperature and (d) salinity observations for the duration of the experiment, and (e) the number of in situ observations per assimilation cycle.

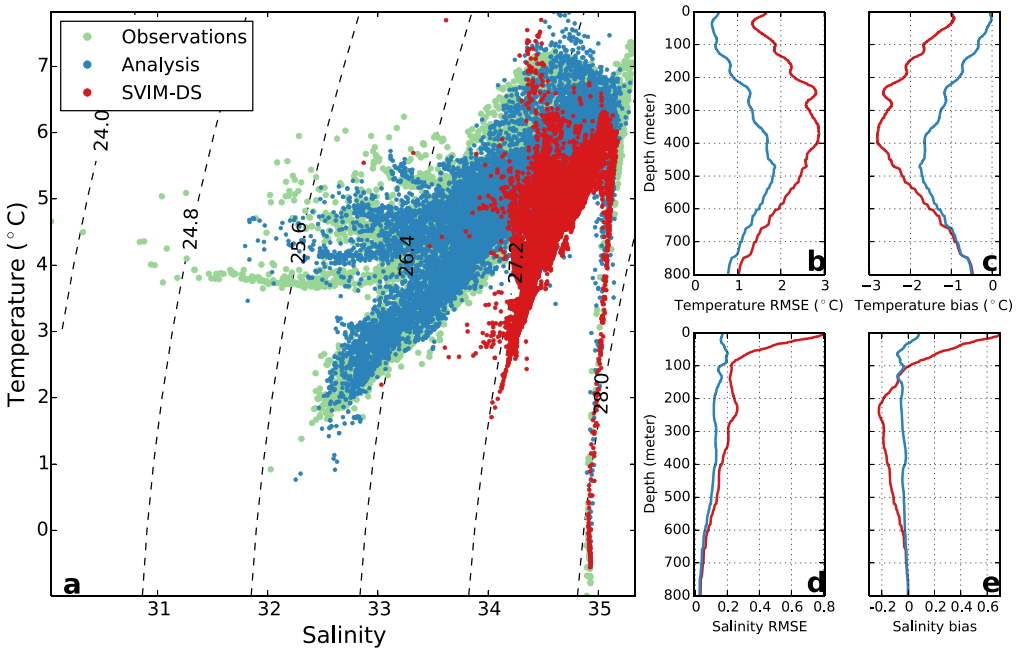

Figure 3. (a) TS-diagram showing the water masses in the observation data set (green), and the corresponding model values for the re-analysis (blue) and SVIM-DS (red). The smaller plots at the right show the models RMSE and bias for (b and c) temperature and (d and e) salinity as a function of depth.

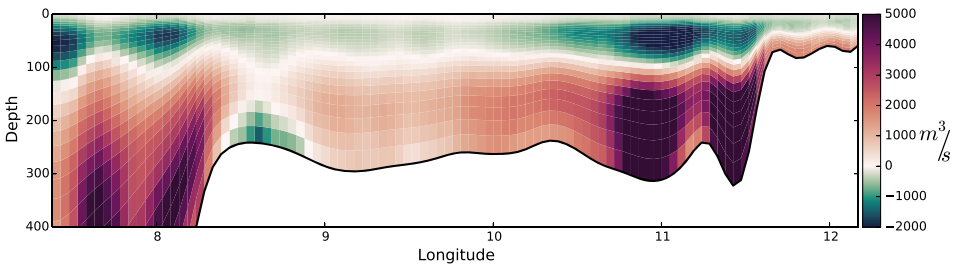

Figure 4. The difference in mean salinity flux through the southern boundary for the period 25 March to 10 April (ANA–SVIM-DS).

The ANA simulation, on the other hand, has a much better representation of the water masses, demonstrating that the analysis scheme has brought the model much closer to the observations. With the exception of extreme salinity values, the reanalysis is able to reproduce the observed water masses with a realistic variation in density. The salinity bias from SVIM-DS is much reduced at all depths, particularly in the upper 100 m. A negative temperature bias still persists below the surface layer, but the bias is reduced by approximately 1°C at all depths above 400 m and the RMSE is decreased by a similar magnitude. For both simulations, the errors in the deeper parts are associated with errors in the lateral boundary conditions.

It is interesting to note the impact of adjusting the boundary conditions through the analysis scheme. Figure 4 shows the average difference between ANA and SVIM-DS in the salinity flux through the southern boundary during a two week period when in situ observations are abundant. The salinity flux is here taken as

$$\overline{F_s} = \overline{\oint uS\,dA}, \tag{2}$$

where u is the normal velocity component at the boundary, S is the salinity, and A is the grid cell area. Most salinity observations are too far away to directly affect the salinity at the boundary given the background error covariances we provide, hence the salinities at the boundary hardly differ between the two simulations. Compared to SVIM-DS, the salinity flux in ANA is decreased in the surface layer and increased in the deeper parts primarily through changes in the velocities at the boundary, and these changes contribute to maintaining a stronger stratification in the reanalysis.

4.2. Baroclinic Dynamics

The above comparison between ANA and SVIM-DS demonstrates a significant difference in the stratification, hence we now evaluate the impact of the state estimation on the first baroclinic Rossby radius of deformation, R_1. Since R_1 is the scale at which rotational effects become important, and is closely linked to the scale of boundary currents, fronts, and eddies, any differences between the two simulations are likely to translate into large differences in transport estimates.

The first baroclinic Rossby radius R_1 is defined as

$$R_1 = \frac{c_1}{|f|}, \tag{3}$$

where f is the local Coriolis parameter and c_1 is the phase speed of the first baroclinic mode internal gravity wave. The phase speed can be found as a solution of an eigenvalue problem, but we will use an approximate WKB solution [*Chelton et al*., 1998]. Thus, we use the following relation:

$$R_1 \approx R_1^{WKB} = \frac{1}{|f|\pi}\int_{-H}^{0} N(z)dz, \tag{4}$$

where H is the local water depth and N is the buoyancy frequency. It should be noted that *Nurser and Bacon* [2014] and *Osinski et al*. [2010], estimating values of R_1 in the Arctic and Baltic, found the WKB approximation to underestimate R_1, particularly in shallow areas. It is thus likely (and more exact solutions not shown

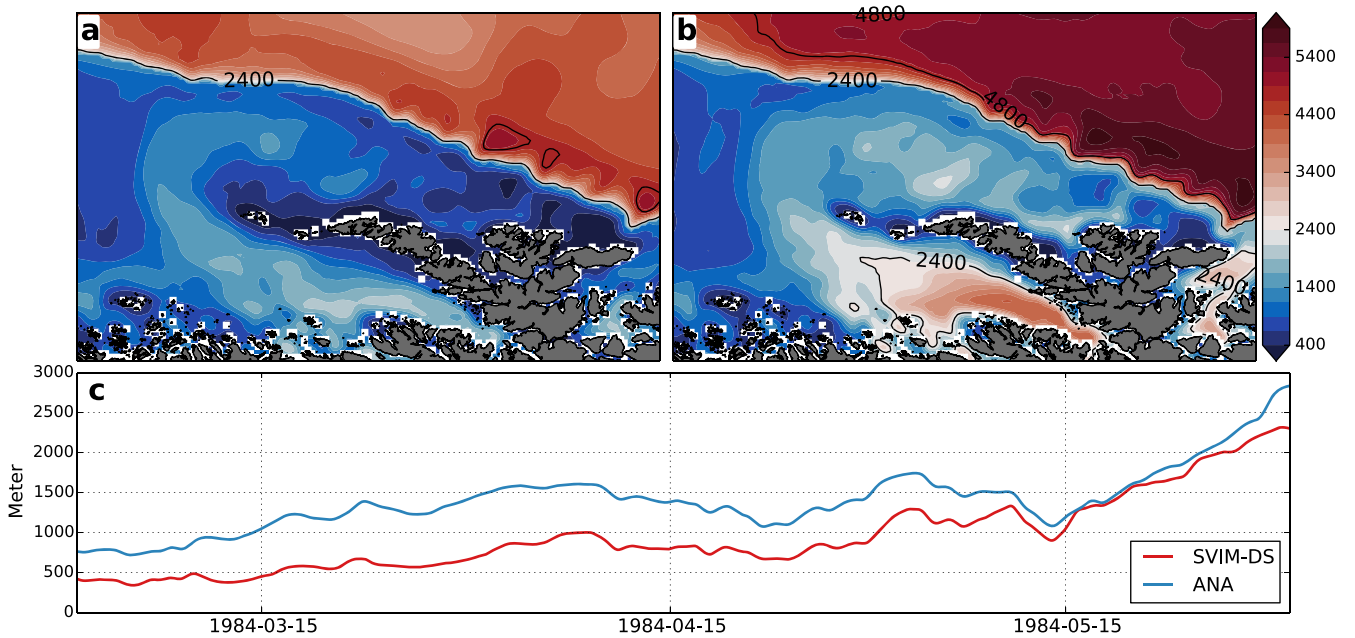

Figure 5. Spring season mean of R_1 for (a) SVIM-DS and (b) ANA with values lower than the horizontal model resolution in blue tones and higher values in reds. (c) A time series of average on-shelf values of R_1.

here support this) that the results presented here yield smaller values of R_1 compared to a solution of the full eigenvalue problem.

Figures 5a and 5b shows the average R_1 over the spring months calculated from the two model simulations. Since the variations of the Coriolis parameter are small in our case, variations in R_1 can primarily be attributed to changes in the depth and the stratification. As a consequence, the shelf break is clearly distinguishable in the results, marking a sharp transition from low to high R_1 values.

For the purposes of this discussion, we define $R_1 > 2\Delta x$ as eddy-resolving and $\Delta x < R_1 < 2\Delta x$ as eddy-permitting, where Δx is the horizontal resolution of our model. It is clear that neither of the simulations are eddy-resolving on the shelf. Over the deep basin, however, ANA is eddy-resolving, while SVIM-DS remains eddy-permitting. ANA also has higher values of R_1 on the shelf, which is particularly evident inside Vestfjorden, where the model now is eddy-permitting, and outside the Lofoten archipelago where the average R_1 values approach the horizontal resolution of the model.

As R_1 depends on the stratification, it exhibits a seasonal cycle. The lowest values are found in March, at the end of the winter season when stratification is weak, and the highest values during summer when there is an increase in runoff due to snow melt and also high insolation. This seasonal cycle seems to be well reproduced by both ANA and SVIM-DS (see Figure 5c), with a shelf-average ($H < 500$ m) of R_1 that slowly increases during the spring, before a rapid increase in mid-May caused by snow melt. The shelf average of R_1 is approximately 500 m larger in ANA throughout the period, indicating that the effective model resolution is increased as a result of the state estimation.

4.3. Upper Ocean Transport

The upper ocean velocities depend on the stratification through the baroclinic response, and in this section statistics of the upper ocean Eulerian and Lagrangian velocities are presented.

Figure 6 shows histograms of Eulerian surface current speeds. The main plot (a) shows histograms based on data from the full model domain and the inlet plots (b–d) show histograms based on data from three subdomains. For the full model domain, the distributions of surface current speeds differ only slightly between ANA and SVIM-DS. Low current speeds occur more frequently in SVIM-DS, while intermediate speeds (0.3–0.5 ms^{-1}) are more frequent in ANA. SVIM-DS has a slightly higher occurrence of velocities above 0.6 ms^{-1}, probably caused by a stronger degree of topographical steering. While the distributions of ANA and SVIM-

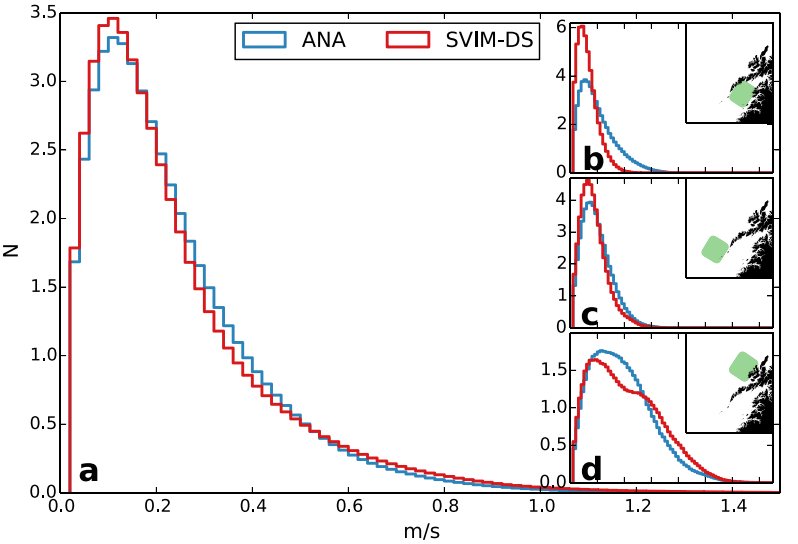

Figure 6. Normalized frequency of occurrence for Eulerian surface current speeds during spring season, obtained from the uppermost model layer that has a thickness of 0.7 m on average. (a) For the full model domain. (b–d) For the subdomains indicated in green. The *x* axes have the same range in all plots.

DS are rather similar when averaged over the entire model domain, the comparisons between subdomains reveal some interesting differences. Inside Vestfjorden (Figure 6b), the surface currents are much more energetic in the reanalysis ANA. Outside Vesterålen (Figure 6d), where the shelf is very narrow, SVIM-DS has a tendency toward a bimodal distribution. The highest speeds are associated with the topographically steered currents along the shelf break, which become more pronounced in SVIM-DS since the surface currents over the deep basins are weak. In ANA, on the other hand, there is no such bimodality and no clear separation between the currents along the shelf break and over the deep basin.

Lagrangian velocities have been obtained by seeding numerical drifters into the Eulerian velocity fields using the OpenDrift trajectory model (https://github.com/OpenDrift/) [*Jones et al.*, 2016]. The drifters were kept at a constant depth of 1 m. A total number of 7680 (288 each third day for 80 days during spring season) numerical drifters were seeded on a uniform grid with 12 km spacing, covering the entire model domain within 30 grid points from the model boundary. Each drifter was active for 256 h (10.6 days). Drifters that stranded or left the model domain within 10.6 days have been removed from the analysis.

Histograms of the drifter speeds are shown in Figure 7. The average Lagrangian drift speeds for both ANA and SVIM-DS are higher (0.42 and 0.35 ms^{-1}, respectively) than their Eulerian counterparts (0.22 and 0.22 ms^{-1}, respectively, compare with Figure 6a). Also, the reanalysis ANA has a much higher occurrence of high Lagrangian drift speeds than SVIM-DS, despite the fact that ANA and SVIM-DS have similar distributions for the Eulerian speeds.

To further investigate the differences between Eulerian and Lagrangian velocities, rotary spectra from both data sets have been calculated. To obtain the Eulerian rotary spectra, hourly surface velocity fields were divided into 512 h long segments, using every 10th grid point to provide some degree of decorrelation between the segments. The rotary spectra for each segment were calculated following *Gonella* [1972], and all the segments were averaged. Figure 8a shows the energy levels of the negative frequency components, which represent anticyclonic motion. SVIM-DS and ANA have approximately the same level of energy at most frequencies, with distinct peaks near the inertial frequency and at the M2 tidal frequency. Figure 8b shows the energy levels of the positive frequency components that represent cyclonic motion. The sharp peak around the M2 frequency is the most dominant feature. SVIM-DS and ANA again have similar energy levels at most frequencies. At higher frequencies (near the Nyquist frequency), the SVIM-DS model is more energetic than ANA in both the negative and positive component spectra. It is not clear to us what is causing this difference, but we speculate whether it can be attributed to the suppression of numerical instabilities being slightly different in the two simulations.

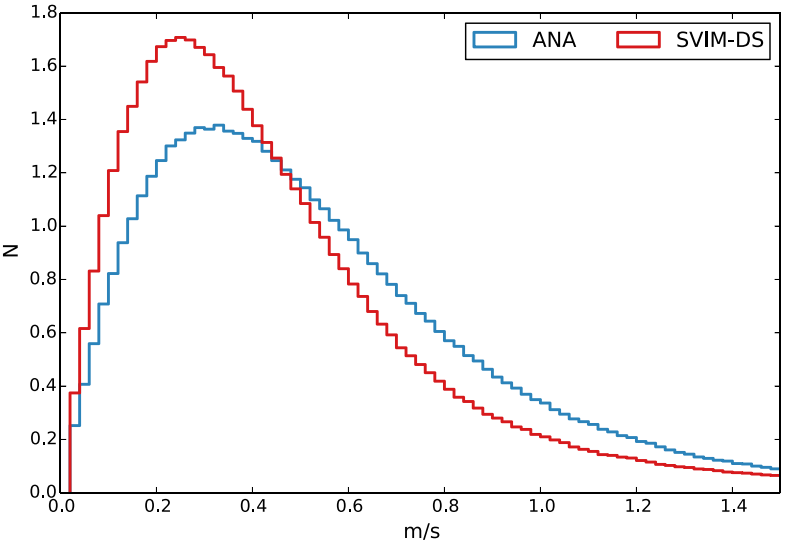

Figure 7. Normalized frequency of occurrence for Lagrangian surface current speed, obtained from artificial model drifters at 1 m depth released during spring season.

Lagrangian rotary spectra were calculated from the velocities of the numerical drifters, using the methodology in *Röhrs and Christensen* [2015]. Each drifter trajectory has a sampling frequency of 0.5 h and a duration of 256 h. The spectra for each segment are averaged to provide the Lagrangian rotary spectra shown in Figure 9a. The spectra compare well with the results obtained for observed drifters in *Röhrs and Christensen* [2015], indicating a realistic representation of upper ocean currents in the model simulations. We note that the Lagrangian energy levels are higher for ANA than for SVIM-DS, although this is not the case for the Eulerian rotary spectra. Figure 9b shows the ratio between the SVIM-DS and ANA energy levels for the positive and negative frequencies, respectively. The differences are highest in the superinertial frequency band where ANA is up to twice as energetic as SVIM-DS, indicating that ANA has more near-inertial oscillations.

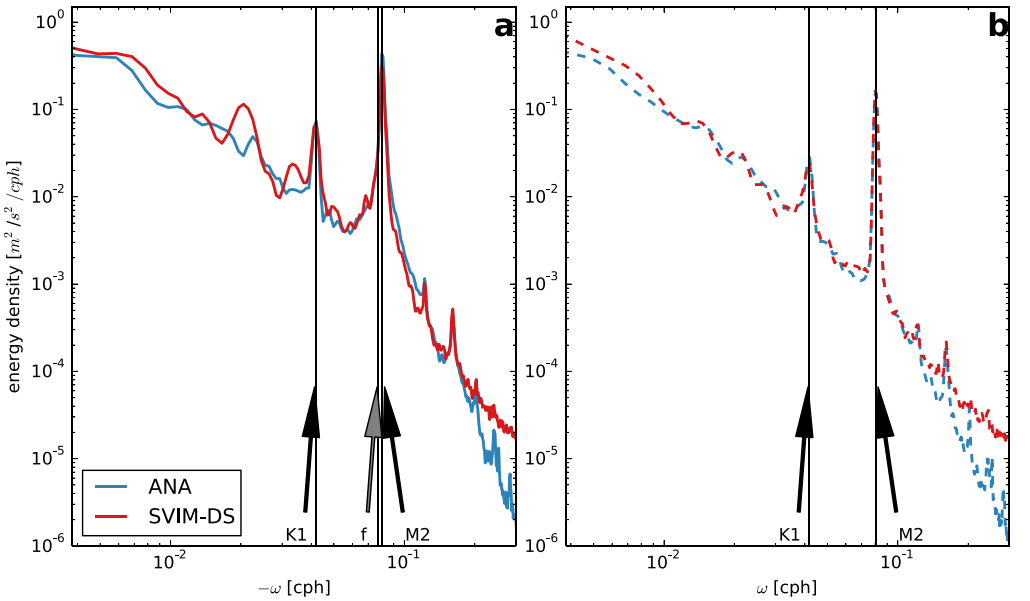

Figure 8. Rotary spectra of Eulerian surface currents. (a) Anticyclonic rotary components and (b) cyclonic rotary components. The vertical bars indicate the lunar tides K1 and M2, and the inertial period f.

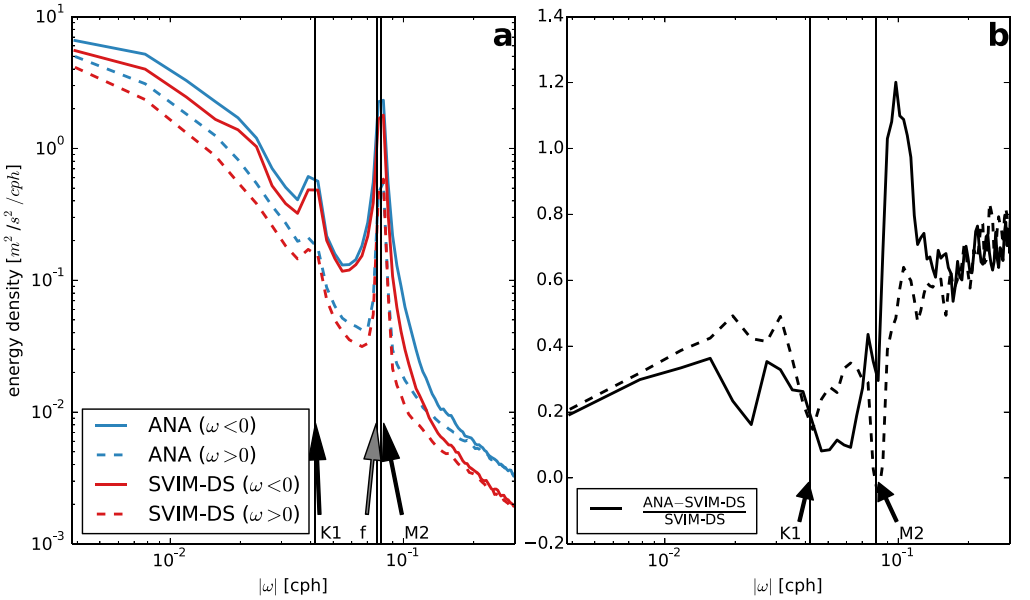

Figure 9. (a) Rotary spectra of Lagrangian surface currents, obtained from the trajectories of artificial model drifters. Anticyclonic rotary components are shown using solid lines and cyclonic rotary components using dashed lines. (b) Difference of rotary components between ANA and SVIM-DS model runs, normalized by SVIM-DS rotary components. Anticyclonic difference is shown using a solid line and cyclonic difference using a dashed line.

5. Discussion and Concluding Remarks

In this study, we have compared a downscaled version of the hindcast archive SVIM with a data assimilative equivalent, both simulating the circulation in the Lofoten/Vesterålen area during the spring of 1984. The SVIM archive has previously been used to study plankton transport and connectivity, but biases in the modeled salinity and temperature are likely to have influenced the results. The assimilation of satellite SST and in situ salinity and temperature brings the reanalysis much closer to the observations, and the distribution of water masses becomes more realistic. It is clear that including the boundary conditions in the control variable vector is beneficial. In our case part of the salinity bias in the interior of the model domain is removed through adjustment of the depth-dependent velocities at the southern boundary.

There are still biases in the reanalysis, in particular a cold bias in the deeper layers, but the reductions are significant in the upper part of the ocean. A recommendation for future research cruises is therefore to collect more hydrography profiles that extend to the bottom. The internal deformation radius (first baroclinic mode) is generally higher in the reanalysis compared to the downscaled hindcast. This increase results in a higher effective resolution in the reanalysis, and is a direct consequence of the improved representation of the stratification. The estimates of the deformation radius indicate, however, that the horizontal resolution of 2.4 km that we have used is too coarse to properly resolve baroclinic instabilities.

The distributions of the Eulerian speeds in the two model simulations are similar, with some local differences that point to the impact of assimilation on the model hydrography. For instance, inside Vestfjorden the speed distribution of the reanalysis is wider, indicating that the currents have become more variable and responsive to the local wind forcing. On the shelf, the downscaled hindcast has a bimodal distribution, with the higher speeds dominated by the strong topographically trapped flow along the shelf break. The reanalysis shows no such tendency toward a bimodal distribution, which again indicates that the currents have become more variable and less dependent on model bathymetry.

We find distinct differences between the reanalysis and the downscaled hindcast when we investigate the energy spectra of Lagrangian drift currents. The energy levels of the reanalysis are generally larger for all frequencies. The differences are particularly large in the superinertial frequency band for the anticyclonic drift velocity components, which indicates a different response to the wind forcing and more intense near-inertial oscillations in the upper layers. One likely cause for these differences is the fact that the more

pronounced stratification in ANA enables a stronger near-surface amplitude of wind-forced currents, as discussed in *Röhrs and Christensen* [2015]. Our analysis does not reveal why the Lagrangian energy levels are higher in the reanalysis, but there are two possible explanations: (i) the differences in the upper ocean dynamics leads to more clustering, and convergence of numerical drifters in regions of strong divergence [*Jacobs et al*., 2016], and/or (ii) the increase in periodic flow features (cf. the increase in the superinertial frequency band) leads to an increase in the residual drift currents [*Longuet-Higgins*, 1969; *Wei et al*., 2004]. A detailed analysis of this issue is outside the scope of the present paper and will be the focus of future investigations.

In this study we have used numerical drifters at a fixed depth of 1 m, thus only evaluating the impact of improved stratification on the currents. For the case of transport of buoyant particles, such as cod eggs and oil droplets, the effect may be even more profound as the particles are likely to have different vertical distributions in the two simulations as a consequence of density differences and its effect on mixing.

Acknowledgments
The model results are available at http://thredds.met.no/thredds/catalog/metusers/LoVe/catalog.html. The NORA10 data used here are available on request to the Norwegian Meteorological Institute, while the SVIM archive is available at ftp://ftp.met.no/projects/SVIM-public/. We gratefully acknowledge financial support from the Research Council of Norway through grants 244262 (RETROSPECT) and 237906 (CIRFA). This research was also supported with computational resources provided by NOTUR (project NN9197K). We would also like to thank Svein Sundby and Frode Vikebø (IMR, Norway), Johnny Johannessen (NERSC, Norway), and Andrew Moore (UCSC, USA) for stimulating and fruitful discussions.

References

Ådlandsvik, B., and S. Sundby (1994), Modelling the transport of cod larvae from the Lofoten area, *ICES Mar. Sci. Symp.*, *198*, 379–392.
Beldring, S., K. Engeland, L. A. Roald, N. R. Sælthun, and A. Voksø (2001), Estimation of parameters in a distributed precipitation-runoff model for Norway, *Hydrol. Earth Syst. Sci.*, *7*(3), 304–316, doi:10.5194/hess-7-304-2003.
Chapman, D. C. (1985), Numerical treatment of cross-shelf open boundaries in a barotropic coastal ocean model, *J. Phys. Oceanogr.*, *15*(8), 1060–1075, doi:10.1175/1520-0485(1985)015 < 1060:NTOCSO>2.0.CO;2.
Chelton, D. B., R. A. deSzoeke, M. G. Schlax, K. El Naggar, and N. Siwertz (1998), Geographical variability of the first baroclinic Rossby radius of deformation, *J. Phys. Oceanogr.*, *28*(3), 433–460, doi:10.1175/1520-0485(1998)028 < 0433:GVOTFB>2.0.CO;2.
Courtier, P., J.-N. Thépaut, and A. Hollingsworth (1994), A strategy for operational implementation of 4d-Var, using an incremental approach, *Q. J. R. Meteorol. Soc.*, *120*(519), 1367–1387, doi:10.1002/qj.49712051912.
De Hoop, L., O. J. Broch, A. J. Hendriks, and F. De Laender (2016), Crude oil affecting the biomass of the marine copepod Calanus finmarchicus: Comparing a simple and complex population model, *Mar. Environ. Res.*, *119*, 197–206, doi:10.1016/j.marenvres.2016.06.008.
Egbert, G. D., and S. Y. Erofeeva (2002), Efficient inverse modeling of barotropic ocean tides, *J. Atmos. Oceanic Technol.*, *19*(2), 183–204, doi:10.1175/1520-0426(2002)019<0183:EIMOBO>2.0.CO;2.
Eide, M. S., Ø. Endresen, Ø. Breivik, O. W. Brude, I. H. Ellingsen, K. Røang, J. Hauge, and P. O. Brett (2007), Prevention of oil spill from shipping by modelling of dynamic risk, *Mar. Pollut. Bull.*, *54*(10), 1619–1633, doi:10.1016/j.marpolbul.2007.06.013.
Ellertsen, B., G. Furnes, P. Solemdal, and S. Sundby (1981), Effects of upwelling on the distribution of cod eggs and zooplankton in Vestfjorden., in *Proceedings from Norwegian Coastal Current Symposium, Geilo, Norway, 9–12 September 1980*, edited by R. Sætre and M. Mork, pp. 604–628, Univ. of Bergen, Bergen, Norway.
Flather, R. A. (1976), A tidal model of the north-west European continental shelf, *Mem. Soc. R. Sci. Liege*, *10*(6), 14–164.
Furnes, G., and S. Sundby (1981), Upwelling and wind induced circulation in vestfjorden, in *Proceedings from Norwegian Coastal Current Symposium, Geilo, Norway, 9–12 September 1980*, edited by R. Sætre and M. Mork, pp. 152–178, Univ. of Bergen, Bergen, Norway.
Gonella, J. (1972), A rotary-component method for analysing meteorological and oceanographic vector time series, *Deep Sea Res. Oceanogr. Abstr.*, *19*(12), 883–846.
Good, S. A., M. J. Martin, and N. A. Rayner (2013), EN4: Quality controlled ocean temperature and salinity profiles and monthly objective analyses with uncertainty estimates, *J. Geophys. Res. Oceans*, *118*, 6704–6716, doi:10.1002/2013JC009067.
Haidvogel, D. B., et al. (2008), Ocean forecasting in terrain-following coordinates: Formulation and skill assessment of the Regional Ocean Modeling System, *J. Comput. Phys.*, *227*(7), doi:10.1016/j.jcp.2007.06.016.
Høyer, J. L., and J. She (2007), Optimal interpolation of sea surface temperature for the North Sea and Baltic Sea, *J. Mar. Syst.*, *65*, 176–189, doi:10.1016/j.jmarsys.2005.03.008.
Isachsen, P. E. (2015), Baroclinic instability and the mesoscale eddy field around the Lofoten Basin, *J. Geophys. Res. Oceans*, *120*, 2884–2903, doi:10.1002/2014JC010448.
Jacobs, G. A., H. S. Huntley, A. D. Kirwan, B. L. Lipphardt, T. Campbell, T. Smith, K. Edwards, and B. Bartels (2016), Ocean processes underlying surface clustering, *J. Geophys. Res. Oceans*, *121*, 180–197, doi:10.1002/2015JC011140.
Janeković, I., B. S. Powell, D. Matthews, M. A. McManus, and J. Sevadjian (2013), 4d-Var data assimilation in a nested, coastal ocean model: A Hawaiian case study, *J. Geophys. Res. Oceans*, *118*, 5022–5035, doi:10.1002/jgrc.20389.
Jones, C. E., K.-F. Dagestad, Ø. Breivik, B. Holt, J. Röhrs, K. H. Christensen, M. Espeseth, C. Brekke, and S. Skrunes (2016), Measurement and modeling of oil slick transport, *J. Geophys. Res. Oceans*, *121*, 7759–7775, doi:10.1002/2016JC012113.
Kvile, K. Ø., Ø. Langangen, I. Prokopchuk, N. C. Stenseth, and L. C. Stige (2016), Disentangling the mechanisms behind climate effects on zooplankton, *Proc. Natl. Acad. Sci. U. S. A.*, *113*(7), 1841–1846, doi:10.1073/pnas.1525130113.
Langangen, Ø., G. Ottersen, L. Ciannelli, F. B. Vikebø, and L. C. Stige (2016), Reproductive strategy of a migratory fish stock: Implications of spatial variations in natural mortality, *Can. J. Fish. Aquat. Sci.*, *73*, 1–8, doi:10.1139/cjfas-2015-0321.
Lien, V. S., Y. Gusdal, J. Albretsen, A. Melsom, and F. B. Vikebø (2013), Evaluation of a Nordic Seas 4 km numerical ocean model hindcast archive (SVIM), 1960–2011, in *Fisken og Havet*, pp. 7–79, Institute of marine research, Bergen, Norway.
Lien, V. S., Y. Gusdal, and F. B. Vikebø (2014), Along-shelf hydrographic anomalies in the Nordic Seas (1960–2011): Locally generated or advective signals?, *Ocean Dyn.*, *64*(7), 1047–1059, doi:10.1007/s10236-014-0736-3.
Longuet-Higgins, M. S. (1969), On the transport of mass by time-varying ocean currents, *Deep Sea Res. Oceanogr. Abstr.*, *16*(5), 431–447, doi:10.1016/0011-7471(69)90031-X.
Marchesiello, P., J. C. McWilliams, and A. Shchepetkin (2001), Open boundary conditions for long-term integration of regional oceanic models, *Ocean Modell.*, *3*, 1–20, doi:10.1016/S1463-5003(00)00013-5.
Moe, H., A. Ommundsen, and B. Gjevik (2002), A high resolution tidal model for the area around The Lofoten Islands, northern Norway, *Cont. Shelf Res.*, *22*(3), 485–504, doi:10.1016/S0278-4343(01)00078-4.

Moore, A. M., H. G. Arango, E. Di Lorenzo, B. D. Cornuelle, A. J. Miller, and D. J. Neilson (2004), A comprehensive ocean prediction and analysis system based on the tangent linear and adjoint of a regional ocean model, *Ocean Modell.*, *7*, 227–258, doi:10.1016/j.ocemod.2003.11.001.

Moore, A. M., H. G. Arango, G. Broquet, B. S. Powell, A. T. Weaver, and J. Zavala-Garay (2011a), The Regional Ocean Modeling System (ROMS) 4-dimensional variational data assimilation systems: Part I: System overview and formulation, *Prog. Oceanogr.*, *91*(1), 34–49, doi:10.1016/j.pocean.2011.05.004.

Moore, A. M., H. G. Arango, G. Broquet, C. Edwards, M. Veneziani, B. Powell, D. Foley, J. D. Doyle, D. Costa, and P. Robinson (2011b), The Regional Ocean Modeling System (ROMS) 4-dimensional variational data assimilation systems: Part II: Performance and application to the California Current System, *Prog. Oceanogr.*, *91*(1), 50–73, doi:10.1016/j.pocean.2011.05.003.

Moore, A. M., H. G. Arango, G. Broquet, C. Edwards, M. Veneziani, B. Powell, D. Foley, J. D. Doyle, D. Costa, and P. Robinson (2011c), The Regional Ocean Modeling System (ROMS) 4-dimensional variational data assimilation systems: Part III: Observation impact and observation sensitivity in the California Current System, *Prog. Oceanogr.*, *91*(1), 74–94, doi:10.1016/j.pocean.2011.05.005.

Myksvoll, M. S., K.-M. Jung, J. Albretsen, and S. Sundby (2014), Modelling dispersal of eggs and quantifying connectivity among Norwegian coastal cod subpopulations, *ICES J. Mar. Sci.*, *71*(4), 957–969, doi:10.1093/icesjms/fst022.

Nurser, A. J. G., and S. Bacon (2014), The Rossby radius in the Arctic Ocean, *Ocean Sci.*, *10*(6), 967–975, doi:10.5194/os-10-967-2014.

Osinski, R., D. Rak, W. Walczowski, and J. Piechura (2010), Baroclinic Rossby radius of deformation in the southern Baltic sea, *Oceanologia*, *52*(3), 417–429.

Poulain, P.-M., A. Warn-Varnas, and P. P. Niiler (1996), Near-surface circulation of the Nordic seas as measured by Lagrangian drifters, *J. Geophys. Res.*, *101*(C8), 18,237–18,258, doi:10.1029/96JC00506.

Reistad, M., Ø. Breivik, H. Haakenstad, O. J. Aarnes, B. R. Furevik, and J.-R. Bidlot (2011), A high-resolution hindcast of wind and waves for the North Sea, the Norwegian Sea, and the Barents Sea, *J. Geophys. Res.*, *116*, C05019, doi:10.1029/2010JC006402.

Reynolds, R. W., T. M. Smith, C. Liu, D. B. Chelton, K. S. Casey, and M. G. Schlax (2007), Daily High-Resolution-Blended Analyses for Sea Surface Temperature, *J. Clim.*, *20*(22), 5473–5496, doi:10.1175/2007JCLI1824.1.

Röhrs, J., and K. H. Christensen (2015), Drift in the uppermost part of the ocean, *Geophys. Res. Lett.*, *42*, 10,349–10,356, doi:10.1002/2015GL066733.

Röhrs, J., K. H. Christensen, F. Vikebø, S. Sundby, Ø. Sætra, and G. Broström (2014), Wave-induced transport and vertical mixing of pelagic eggs and larvae, *Limnol. Oceanogr.*, *59*(4), 1213–1227, doi:10.4319/lo.2014.59.4.1213.

Shchepetkin, A. F., and J. C. McWilliams (2005), The regional oceanic modeling system (ROMS): A split-explicit, free-surface, topography-following-coordinate oceanic model, *Ocean Modell.*, *9*(4), 347–404, doi:10.1016/j.ocemod.2004.08.002.

Sperrevik, A. K., K. H. Christensen, and J. Röhrs (2015), Constraining energetic slope currents through assimilation of high-frequency radar observations, *Ocean Sci.*, *11*(2), 237–249, doi:10.5194/os-11-237-2015.

Stige, L. C., Ø. Langangen, N. A. Yaragina, F. B. Vikebø, B. Bogstad, G. Ottersen, N. C. Stenseth, and D. Ø. Hjermann (2015), Combined statistical and mechanistic modelling suggests food and temperature effects on survival of early life stages of Northeast Arctic cod (Gadus morhua), *Prog. Oceanogr.*, *134*, 138–151, doi:10.1016/j.pocean.2015.01.009.

Sundby, S., and P. Bratland (1987), Kartlegging av gytefeltene for norsk-arktisk torsk i Nord-Norge og beregning av eggproduksjonen i årene 1983–1985, *Fisken og Havet*, vol. *1*, pp. 1–58.

Svendsen, E., M. Skogen, P. Budgell, G. Huse, J. Erik Stiansen, B. Ådlandsvik, F. Vikebø, L. Asplin, and S. Sundby (2007), An ecosystem modeling approach to predicting cod recruitment, *Deep Sea Res., Part II*, *54*, 2810–2821, doi:10.1016/j.dsr2.2007.07.033.

Vikebø, F., C. Jørgensen, T. Kristiansen, and Ø. Fiksen (2007), Drift, growth, and survival of larval Northeast Arctic cod with simple rules of behaviour, *Mar. Ecol. Prog. Ser.*, *347*, 207–219, doi:10.3354/meps06979.

Vikebø, F. B., P. Rønningen, V. S. Lien, S. Meier, M. Reed, B. Ådlandsvik, and T. Kristiansen (2013), Spatiotemporal overlap of oil spills and early life stages of fish, *ICES J. Mar. Sci.*, *4*, 970–981, doi:10.1093/icesjms/fst131.

Volkov, D. L., A. A. Kubryakov, and R. Lumpkin (2015), Formation and variability of the Lofoten basin vortex in a high-resolution ocean model, *Deep Sea Res., Part I*, *105*, 142–157, doi:10.1016/j.dsr.2015.09.001.

Warner, T. T., R. A. Peterson, and R. E. Treadon (1997), A tutorial on lateral boundary conditions as a basic and potentially serious limitation to regional numerical weather prediction, *Bull. Am. Meteorol. Soc.*, *78*, 2599–2617, doi:10.1175/1520-0477(1997)078 < 2599:ATOLBC>2.0.CO;2.

Wei, H., D. Hainbucher, T. Pohlmann, S. Feng, and J. Suendermann (2004), Tidal-induced Lagrangian and Eulerian mean circulation in the Bohai Sea, *J. Mar. Syst.*, *44*(3–4), 141–151, doi:10.1016/j.jmarsys.2003.09.007.